ORIGINAL ARTICLE

Application of 2D and 3D geoelectrical resistivity imaging for engineering site investigation in a crystalline basement terrain, southwestern Nigeria

Ahzegbobor Philips Aizebeokhai · A. I. Olayinka · V. S. Singh

Abstract Orthogonal set of 2D geoelectrical resistivity field data, consisting of six parallel and five perpendicular profiles, were collected in an investigation site using the conventional Wenner array. Seven Schlumberger soundings were also conducted on the site to provide ID layering information and supplement the orthogonal 2D profiles. The observed 2D apparent resistivity data were first processed individually and then collated into 3D data set which was processed using a 3D inversion code. The 3D model resistivity images obtained from the inversion are presented as horizontal depth slices. Some distortions observed in the 2D images from the inversion of the 2D profiles are not observed in the 2D images extracted from the 3D inversion. The survey was conducted with the aim of investigating the degree of weathering and fracturing in the weathered profile, and thereby ascertaining the suitability of the site for engineering constructions as well as determining its groundwater potential.

Keywords Geoelectrical · Resistivity · Imaging · 2D and 3D inversion · Orthogonal profiles · Engineering investigations

A. P. Aizebeokhai (✉)
Department of Physics, Covenant University, Ota, Nigeria
e-mail: Philips_a_aizebeokhai@yahoo.co.uk

A. I. Olayinka
Department of Geology, University of Ibadan, Ibadan, Nigeria

V. S. Singh
National Geophysical Research Institute, Hyderabad, India

Introduction

Geoelectrical resistivity imaging has played an important role in addressing a wide variety of hydrogeological, environmental and geotechnical issues. The goal of geoelectrical resistivity surveys is to determine the distribution of subsurface resistivity by taking measurements of the potential difference on the ground surface. For a typical inhomogeneous subsurface, the true resistivity distribution is estimated by carrying out inversion on the observed apparent resistivity values. In environmental and engineering investigations, the subsurface geology is usually complex, subtle and multi-scale such that both lateral and vertical variations in the petrophysical properties can be very rapid. Two-dimensional (2D) geoelectrical resistivity imaging has been widely used to map areas with moderately complex geology (e.g. Griffiths and Barker 1993; Griffiths et al. 1990; Dahlin and Loke 1998; Olayinka 1999; Olayinka and Yaramanci 1999; Amidu and Olayinka 2006). In the 2D model of interpretation, the subsurface resistivity is considered to vary both laterally and vertically along the survey line but constant in the perpendicular direction. The major limitation of the 2D geoelectrical resistivity imaging is that measurements made with large electrode spacing are often affected by the deeper sections of the subsurface as well as structures at a larger horizontal distance from the survey line. This is most pronounced when the survey line is placed near a steep contact with the line parallel to the contact (Loke 2001).

Geological structures and spatial distributions of subsurface petrophysical properties and/or contaminants commonly encountered in environmental, hydrogeological and engineering investigations are inherently three-dimensional (3D). Thus, the assumption of the 2D model of interpretation is commonly violated. Images resulting from

2D geoelectrical resistivity surveys can contain spurious features due to 3D effects. This usually leads to misinterpretation and/or misrepresentation of the observed anomalies in terms of magnitude and location; and the 2D images produced are only along the survey lines and not the entire investigation site. Thus, geometrically complex heterogeneities cannot be adequately characterized with vertical electrical sounding or 2D electrical resistivity imaging alone. Hence, a 3D geoelectrical resistivity survey with a 3D model of interpretation, where the resistivity values are allowed to vary in all the three directions, namely vertical, lateral and perpendicular directions, should in theory give a more accurate and reliable results.

In this paper, orthogonal set consisting of six parallel and five perpendicular 2D geoelectrical resistivity imaging profiles, and seven Schlumberger soundings data were conducted, during the raining season, in an investigation site located in the University of Ibadan, southwestern Nigeria. Measurements of the orthogonal 2D profiles were made using the conventional Wenner electrode configuration with the aid of a Campus Tigre resistivity instrument. The observed orthogonal set of 2D apparent resistivity data were collated into 3D data set and then inverted using a 3D inversion code, RES3DINV (Loke and Barker 1996b). The resistivity soundings were conducted to obtain 1D layering information which aids the interpretation of the 2D and 3D geoelectrical resistivity imaging. The survey was conducted, as part of experimental studies to determine the effectiveness of using parallel or orthogonal sets of 2D profiles to generate 3D data set in geoelectrical resistivity imaging, with the aim of determining the suitability of the site for engineering construction and its groundwater potential by investigating the degree of weathering and fracturing in the weathered profile developed above the crystalline basement.

Study area

The campus of the University of Ibadan is located in the north-central part of Ibadan metropolis, southwestern Nigeria. It lies between latitudes 7°26.00′N and 7°26.71′N, and longitude 3°53.00′E and 3°54.12′E (Fig. 1). About half of the total land mass of Nigeria is covered by the Precambrian basement complex rocks introduced by younger granites of Jurassic age. The other half is made up of Cretaceous to Recent sediments overlying the basement rocks. The basement complex rocks in Ibadan area are mainly the metamorphic rocks of Precambrian age with few intrusions of granites and porphyries of Jurassic age. The dominant rock types are quartzites of the meta-sedimentary series and banded gneisses, augen gneisses and migmatites which constitute the gneiss–migmatite

complex. Other associated rock types include pegmatites, quartz, aplites, dolerites dykes, amphibolites, and xenoliths. In most part of Ibadan, the rocks are overlain by the weathered regolith; thus, outcrops are correspondingly few. Banded gneiss constitutes over 75% of the rocks in and around Ibadan while augen gneisses and quartzites share the remaining in about equal percentages.

Expectedly, the University of Ibadan campus is underlain mainly by quartzites and quartz schists, granite gneisses, and augen gneisses (Fig. 1). The western part of the campus is underlain by quartzites and quartz schists, while the augen gneiss occurs in the eastern part. They are separated by the granite gneiss extending northward from the southern part to the point where it terminates. The quartzites, quartz schists and augen gneisses outcrop in various parts of the campus; but the quartzites and quartz are more extensively weathered and fractured. Foliation planes are well developed and the general strike is north–south; the rocks dip easterly with dip values ranging from 10° to 50°.

The area is within the humid tropics with a mean rainfall of 1,237 mm (Akintola 1986). The climate is characterized by two seasons, namely the rainy season (April–October) and the dry season (November–March). Most of the precipitation is received during the rainy season. The campus is drained by River Ona, which is linked by other smaller rivers and flows southwest in the northern part of the campus; the general drainage pattern is trellis. The discharge of the rivers fluctuates with the weather conditions, the highest being recorded during the rainy season, usually between the months of April and October. The water level is usually low from November to February while some of the rivers may be completely dry. Water supply on the campus is pipe borne, and the groundwater is yet to be fully developed. A review of hydrogeological potential of the crystalline basement by Acworth (1987) indicates that the water table in the area is in the neighbourhood of 10 m during the dry season and is expected to be much shallower during the wet season when this survey was carried out. The weathered profile developed above crystalline basement rocks in low latitude regions comprises, from top to bottom, the top soil, the saprolite which is a product of in situ chemical weathering of the bedrock, the saprock (or fractured bedrock) and fresh bedrock.

In general, basement complex rocks are considered to be poor aquifers because of their low porosity and permeability which determines the hydrogeological properties of the rocks depending on the texture and mineralogy of the rocks. In fresh, non-fractured crystalline rocks, the porosity is often less than 3%. However, this can be increased considerably by fracturing. The permeability depends on the degree of interconnectivity of the voids. Invariably, the links/interconnectivities are provided by fractures and

Fig. 1 Geological map of University of Ibadan campus, southwestern Nigeria, showing the location of the study area (after Amidu and Olayinka 2006)
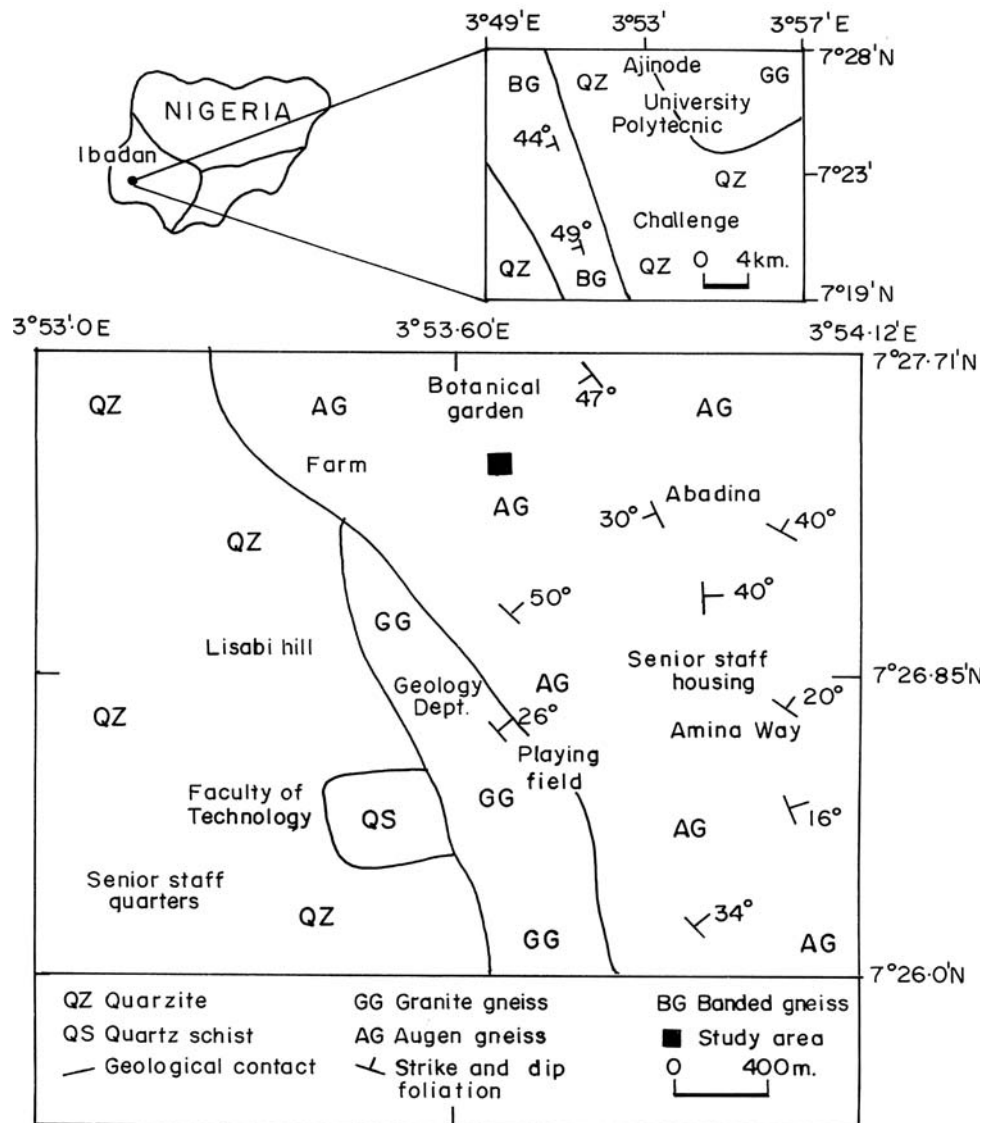
weathered profile. The occurrence and distribution of groundwater in these crystalline units are therefore controlled by the presence and development of integrated fracture system, intensity of fracturing, degree of metamorphic, and the degree and pattern of weathering (Acworth 1987). The extent of weathering is generally limited to rock types. Rocks dominated by unstable ferromagnesian minerals tend to weather into clayey, sometimes micaceous impermeable non-water-bearing rock formation whereas rocks consisting mainly of quartz and other stable minerals will disintegrate into porous and permeable water-bearing gravelly or sandy medium. The weathered layer is of hydrogeological significance not only because of its ability to store water but also serve as a recharge medium for the underlying fracturing unit through percolation of water during precipitation . The attribute of the fracture system also varies with the rock type, zone of intense

shattering and faulting are commonly developed in crystalline rock units. If the fractures are deep enough, both vertical and lateral groundwater movement are favoured. The fractured zones stores water and also act as zone of groundwater flow.

Geoelectrical resistivity imaging survey

A total of 11 multi-electrodes 2D geoelectrical resistivity imaging lines were measured with the aid of a Campus Tigre model resistivity meter using the Wenner-alpha array. The survey was conducted during the raining season. A manual data collection technique was employed. Each of the 2D traverses was 100.0 m in length and they form an orthogonal set such that the total area covered by the 2D traverses is 100×100 m^2. The electrode spacing ranged

from 2.0 to 20.0 m in an interval of 2.0 m, with a total of 51 electrode positions for each traverse line. This gives a total data level of 10 for each traverse so that data points of 345 was observed per traverse line. Six of the 2D traverses denoted as in-lines (Traverse 1–Traverse 6) were conducted parallel to each other, separated by a distance of 20.0 m (i.e. 10a where a is the minimum electrode spacing) from each other, and oriented in the west–east direction. Whereas the other five 2D traverses denoted as cross-lines (Trav. 7–Trav. 11) runs perpendicular to the in-lines and were separated by a distance of 25.0 m (i.e. 12.5a) from each other in the north–south direction. Seven geoelectrical resistivity soundings data were also collected in the site using Schlumberger array to supplement the observed 2D apparent resistivity data and provide layering information on the weathered profile developed above the crystalline basement. Figure 2 shows the survey plan with the locations of the traverses and sounding points.

The measurements commenced at the west end for the in-lines and the north end for the cross-lines with electrode spacing of 2.0 m at electrode positions 1, 2, 3 and 4 in each 2D traverse. Each electrode was then shifted a distance of 2.0 m (one unit electrode spacing), the active electrode positions being 2, 3, 4 and 5. The procedure was continued to the end of the traverse line with electrode positions for the last measurement being 48, 49, 50 and 51. The electrode spacing was then increased by 2.0 m, as noted above, for measurements of the next data level, such that the

active electrode positions were 1, 3, 5 and 7. The procedure was then repeated by shifting each of the electrodes a distance of 2.0 m (one unit electrode spacing) and maintaining the electrode spacing for the data level until the electrodes were at electrode positions 45, 47, 49 and 51. This procedure was continued until 10 data levels were observed, yielding a total of 345 data points in each of the traverses.

The resistivity meter was set on resistance mode and for repeat measurements with a cycle of four stacking. At every data point observation, the resistivity meter displayed resistance value four times before displaying the median value and the corresponding root mean square (RMS) error associated with the reading. These readings were then recorded; the RMS error values were generally less than 2% throughout the survey. Measurements of data points in which the RMS error value was higher were repeated, however, RMS error value of 5% is generally acceptable. The observed resistance values were used to compute the apparent resistivity values.

Data processing and inversion

The vertical electrical soundings (VES) data were processed using Win-Resist computer code to obtain the one-dimensional resistivity models for the site. The apparent resistivity values for each traverse were collated in a format that is acceptable by the RES2DINV inversion code. Elevation corrections were not included in the measurements as the area surveyed was more or less flat. RES2DINV computer code (Loke and Barker 1996a) was used in the inversion of the 2D data. The computer program uses a nonlinear optimization technique which automatically determines a 2D resistivity model of the subsurface for the input apparent resistivity data (Griffiths and Barker 1993; Loke and Barker 1996a). The program divides the subsurface into a number of rectangular blocks according to the spread of the observed data. Least-squares inversion with standard least-squares constraint which attempt to minimize the square of the difference between the observed and the calculated apparent resistivity values was used to invert all the 2D traverses. The smoothness constraint was applied to the model perturbation vector only.

The sensitivity values provide information on the section of the subsurface with the greatest effect on the measured apparent resistivity values. The sensitivity values were normalized by dividing the calculated sensitivity values with the average sensitivity for the particular model configuration. Line search which uses quadratic interpolation to find the optimum step size for the change in apparent resistivity of model blocks was used at each iteration step. Standard Gauss–Newton optimization
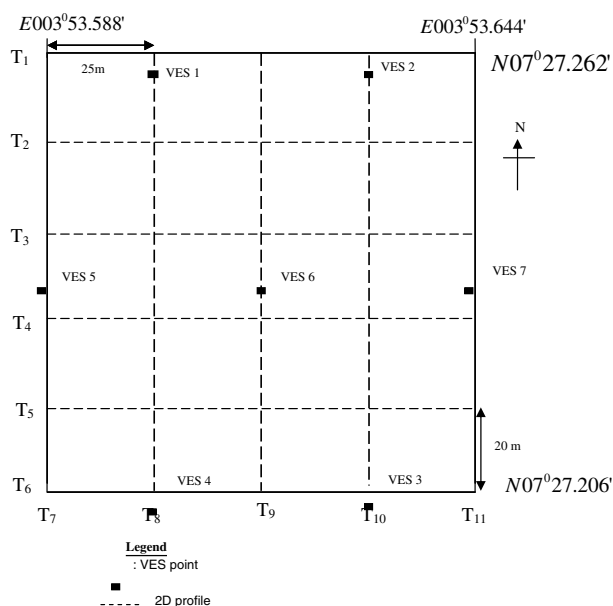

Fig. 2 Geoelectrical resistivity survey plan showing the locations of 2D traverses and VES points for the experimental site located at UI Research Farm, Ibadan, Nigeria. Profiles in the east–west direction are 20 m apart, while profiles in the north–south direction are 25 m apart

method was used, with a convergent limit of 0.005. The Jacobian matrix was recalculated for all iterations; homogeneous half-space was used as initial model. A grid size of 4 nodes per unit electrode and normal mesh were used in the forward modelling subroutine for calculating apparent resistivity values. The initial and minimum damping factor used for the inversion is 0.225 and 0.05, respectively (the default setting is 0.160 and 0.015, respectively). The damping factor was allowed to increase with depth by a factor of 1.05 since the resolution of resistivity decreases exponentially with depth. The damping factor was optimised so as to significantly reduce the number of iterations required for convergence, however, the time taken per iteration increases.

The entire orthogonal set of 2D lines (11 traverses) were merged together to form a single 3D data set. This was done by collating the measured 2D data (apparent resistivity values) to a 3D data format that can be read by the RES3DINV software (Loke and Barker 1996b) using the RES2DINV computer code. The coordinates, line directions, number of electrodes, electrode spacing and data levels of each of the 2D traverses were used in collating the apparent resistivity values with the aid of an input text file which can be read by the computer code. The collation gave rise to a grid size of 53×51 electrodes in the x- and y-directions, respectively. The 2D cross-lines at 25 and 75 m positions accounted for the extra two electrodes in the x-directions, as the electrode positions were evenly spaced 2.0 m apart in both x-direction (in-lines) and y-direction (cross-lines). Thus, the data density for the 3D data set obtained by collating the orthogonal 2D set is 3,795 data points. The in-lines and the cross-lines were also collated into 3D data set separately.

The collated 3D data sets were inverted using RES3DINV computer code which automatically determines a 3D model of resistivity distribution using apparent resistivity data obtained from a 3D resistivity imaging survey (Li and Oldenburg 1994; White et al. 2001). Ideally, the electrodes used for such a survey are arranged in squares or rectangular grids. The inversion routine used by the RES3DINV program is based on the smoothness constrained least-squares method (de Groot-Hedlin and Constable 1990; Sasaki 1992), as in RES2DINV for 2D inversion, though a robust inversion can also be implemented. The smoothness constrained least-squares is based on the following equations:

$$\{J^{T}J + \mu(f_x f_x^{T} + f_z f_z^{T})\}d = J^{T}g, \qquad (1)$$

where f_x is the horizontal flatness, f_z is the vertical flatness, μ is the damping factor, J is the Jacobian matrix of partial derivatives, d is the model perturbation vector, g is the discrepancy vector which contains the differences between the logarithms of the measured and calculated apparent resistivity values, and J^{T} is the transpose of J.

The program allows users to adjust the damping factor and the flatness filters in the equation above to suit the data set being inverted. Initial damping factor of 0.215 was used to invert the collated 3D apparent resistivity data set. After each iterating process, the inversion subroutine generally reduced the damping factor used; a minimum limit (one-tenth of the value of the initial damping factor used) was set to stabilize the inversion process. The damping factor was optimised so as to reduce the number of iterations the program requires to converge by finding the optimum damping factor that gives the least RMS error; however, this increases the time taken per iteration. In order to determine the 3D distribution of the model resistivity values from the distribution of apparent resistivity values, the subsurface was subdivided into a number of small rectangular blocks. The program defunct for the first layer thickness based on the maximum depth of investigation of the array was used and was increased by 1.15 (15%) for subsequent layers. Finite difference grids of three nodes between adjacent electrodes were used. Homogeneous earth model was used as the initial model in the inversions carried out.

Results and discussion

A summary of the VES model resistivity values are presented in Table 1. The VES model resistivity values complement the inversion results of the 2D and 3D resistivity images. The iso-resistivity contour maps of the layers which show the lateral variations of model resistivity values within a given layer are given in Figs. 3, 4, 5. Figure 3 shows that the upper layer is characterized largely by model resistivity values ranging between 100 and 640 Ωm with an average thickness of 0.8 m. Previous studies within the University campus (Amidu and Olayinka 2006) suggest that the upper layer is mainly composed of hard and resistive sandy-silty clay underlain by a less resistive saprolite. From the VES results, the model resistivity values of the second layer (saprolite) is much lower than that of the first and varies between 20 and 95 Ωm as shown in Fig. 4. The average thickness of the saprolite is about 6.6 m. The saprolite overlies a more consolidated and resistive fractured basement rock whose resistivity varies widely between 200 and 1,200 Ωm as shown in Fig. 5 as indicated by the results from the VES.

The 2D resistivity inversion model sections of the in-lines and cross-lines traverses which are perpendicular to each other are presented in Figs. 6 and 7, respectively. The RMS errors achieved in the inversion models were generally less than 5% except for some of the profiles that

Table 1 Summary of VES model resistivity values and their corresponding thicknesses

	Layer 1 (top soil)		Layer 2 (saprolite)		Layer 3 (saprock)		Layer 4 (saprock)	
	Resistivity (Ωm)	Thickness (m)	Resistivity (Ωm)	Thickness (m)	Resistivity (Ωm)	Thickness (m)	Resistivity (Ωm)	Thickness (m)
VES 1	561.9	0.8	93.1	7.8	571.1	3.9	18 927.7	–
VES 2	490.2	1	61.5	7.5	643.1	–	–	–
VES 3	108.1	1	21.0	8.9	328.4	–	–	–
VES 4	631.0	0.6	39.1	3.3	759.2	7.6	206.5	–
VES 5	226.2	0.9	24.9	2.5	2106.0	28.7	366.5	–
VES 6	282.7	0.6	27.5	7.9	746.5	–	–	–
VES 7	215.2	0.8	25.3	8.2	362.7	–	–	–

Fig. 3 Iso-resistivity map of the first layer using the model resistivity values obtained from the VES
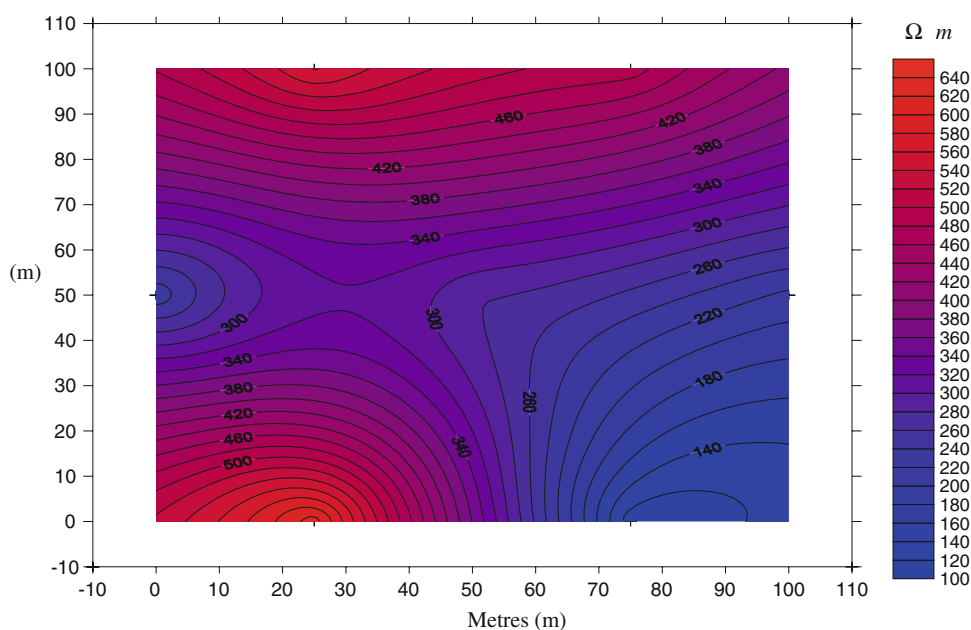
appears relatively noisy. However, there is a reasonable agreement between the inversion model sections of all the profiles. The investigation depth of the 2D images can be approximated into a three-layer model in which the model resistivity of the middle layer (saprolite) is much lower than those of upper and lower layers. This trend is similar to that observed in the iso-resistivity contour maps (Figs. 3, 4, 5) produced from the VES model resistivity values; however, the inversion model sections show a smooth two-dimensional variation in the model resistivity values.

The 3D model resistivity values of the smoothness constrained least-squares inversion are presented as horizontal depth slices in Fig. 8. A RMS error of 17.7% was achieved in the 3D inversion after four iterations. The relative high RMS error is attributed to some mesh cells without data point as a result of the 3D grid created from the orthogonal set of 2D profiles. The different error characteristics associated with the different 2D profiles combined to form the 3D data set could also be responsible

to the high RMS error achieved. In addition, 2D images were extracted from the 3D inversion models (Fig. 9) at locations where the input 2D profiles were conducted. The extracted 2D images are compared directly with the inversion images of the input 2D profiles.

The 2D resistivity images of the in-line profiles show that the saprolite generally thickens towards the east with the model resistivity values decreasing with increasing thickness and ranging from a minimum of about 4 Ωm to a maximum of 50 Ωm. This is in agreement with the inversion model sections of the perpendicular (cross-lines) profiles and the 3D inversion images. In general, the western part of the site is more resistive than the eastern part; and the thickness of the saprolite and the weathered bed rock increases eastward with decreasing resistivity. Thus, the western part of the site is more consolidated and least affected by weathering actions. This also depicts that the groundwater flows eastward in both the vadose zone and in the aquifer system. Hence, boreholes sited in the

Fig. 4 Iso-resistivity map of the second layer using model resistivity values obtained from the VES
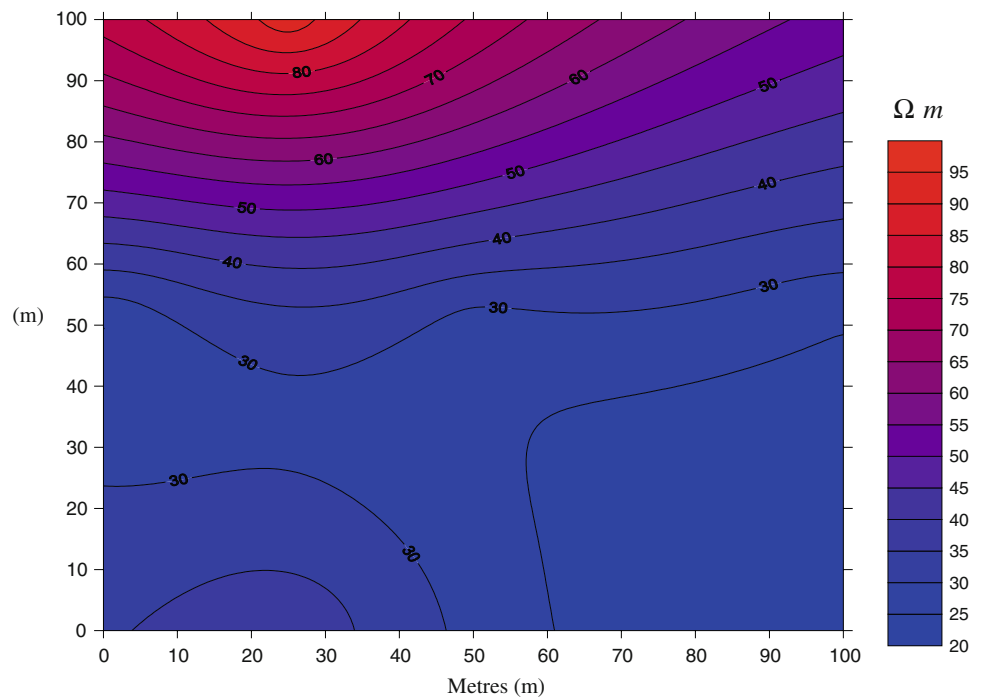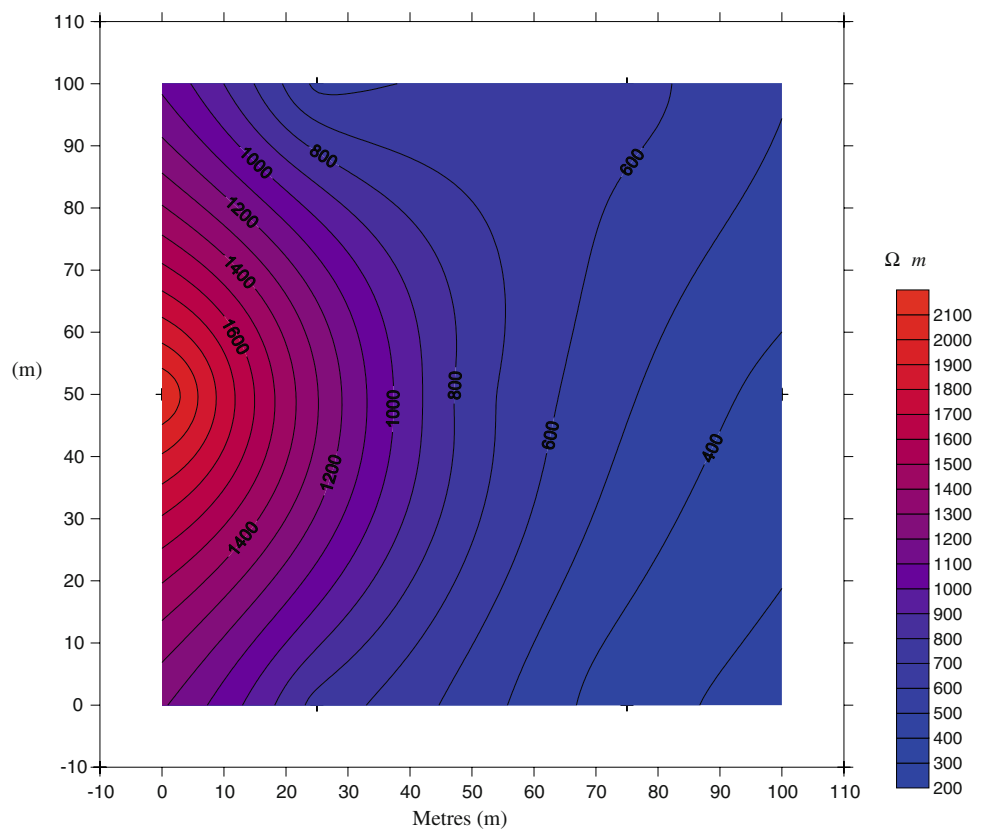

Fig. 5 Iso-resistivity map of the third layer using model resistivity values obtained from the VES

eastern part of the investigation site would be more productive than those sited in the western part. For the same reasons mentioned above, the western part would favour the construction of heavy engineering structures.

Abnormally low and high model resistivity values in the 2D resistivity images have been removed from the 3D inversion images with the 3D model resistivity values ranging from a minimum of about 10 Ωm to a maximum of
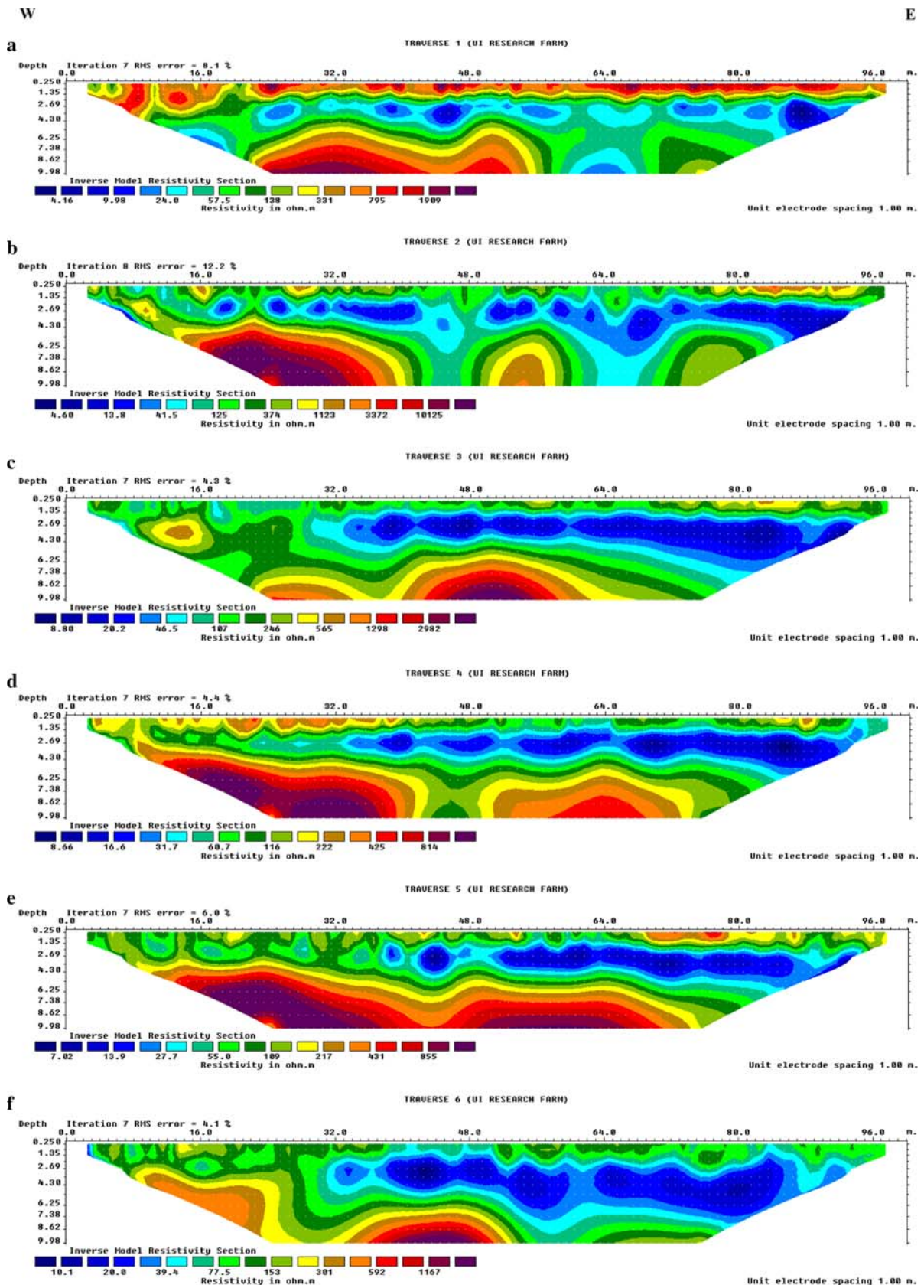
W

E

Fig. 6 Model resistivity section of **a** traverse 1, **b** traverse 2, **c** traverse 3, **d** traverse 4, **e** traverse 5, and **f** traverse 6 in the west–east direction with inter-line spacing of 20 m, using smoothness constrained inversion
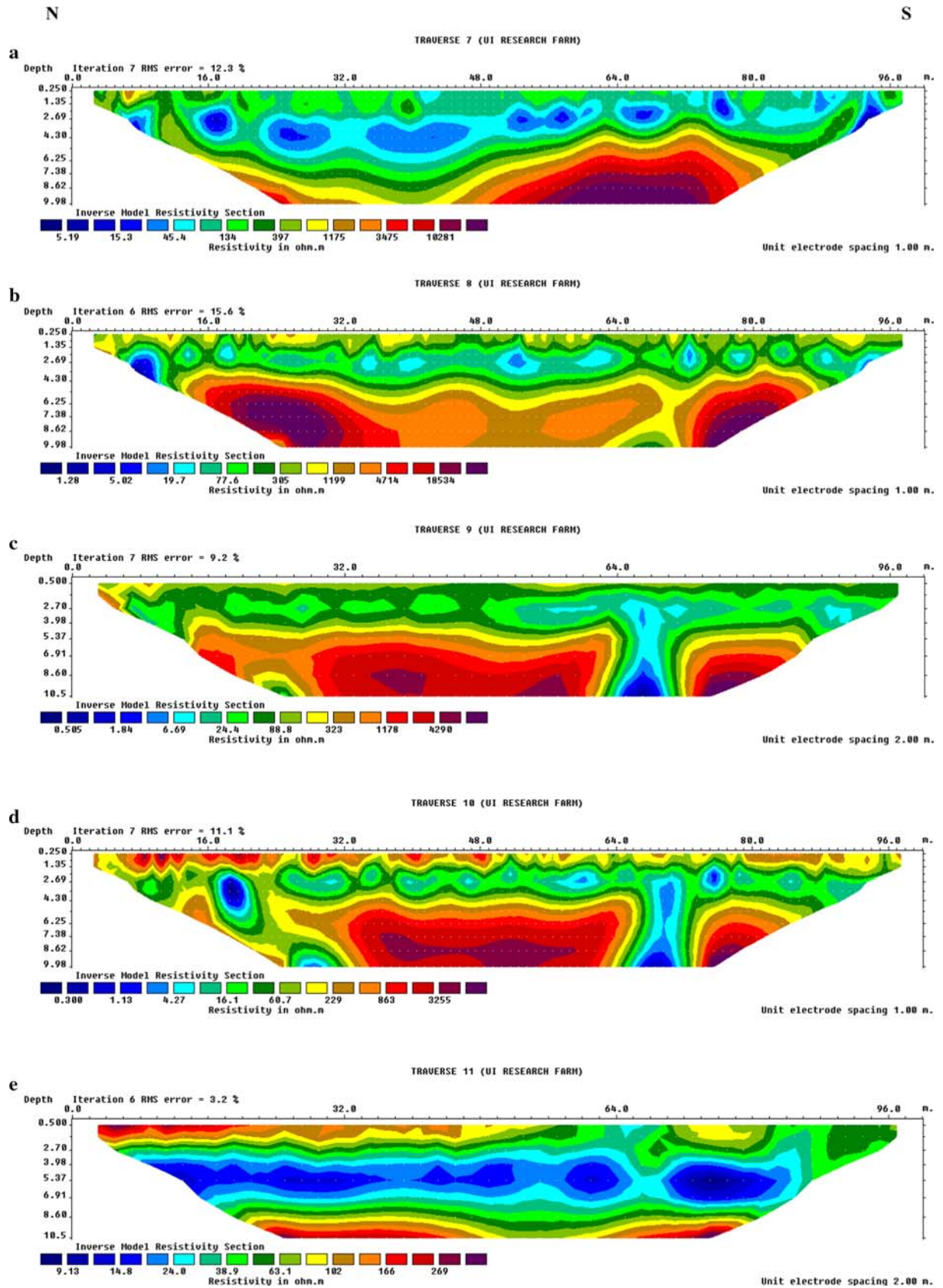
Fig. 7 Model resistivity section of **a** traverse 7, **b** traverse 8, **c** traverse 9, **d** traverse 10, and **e** traverse 11 in the north–south direction with inter-line spacing of 25 m, using smoothness constrained inversion
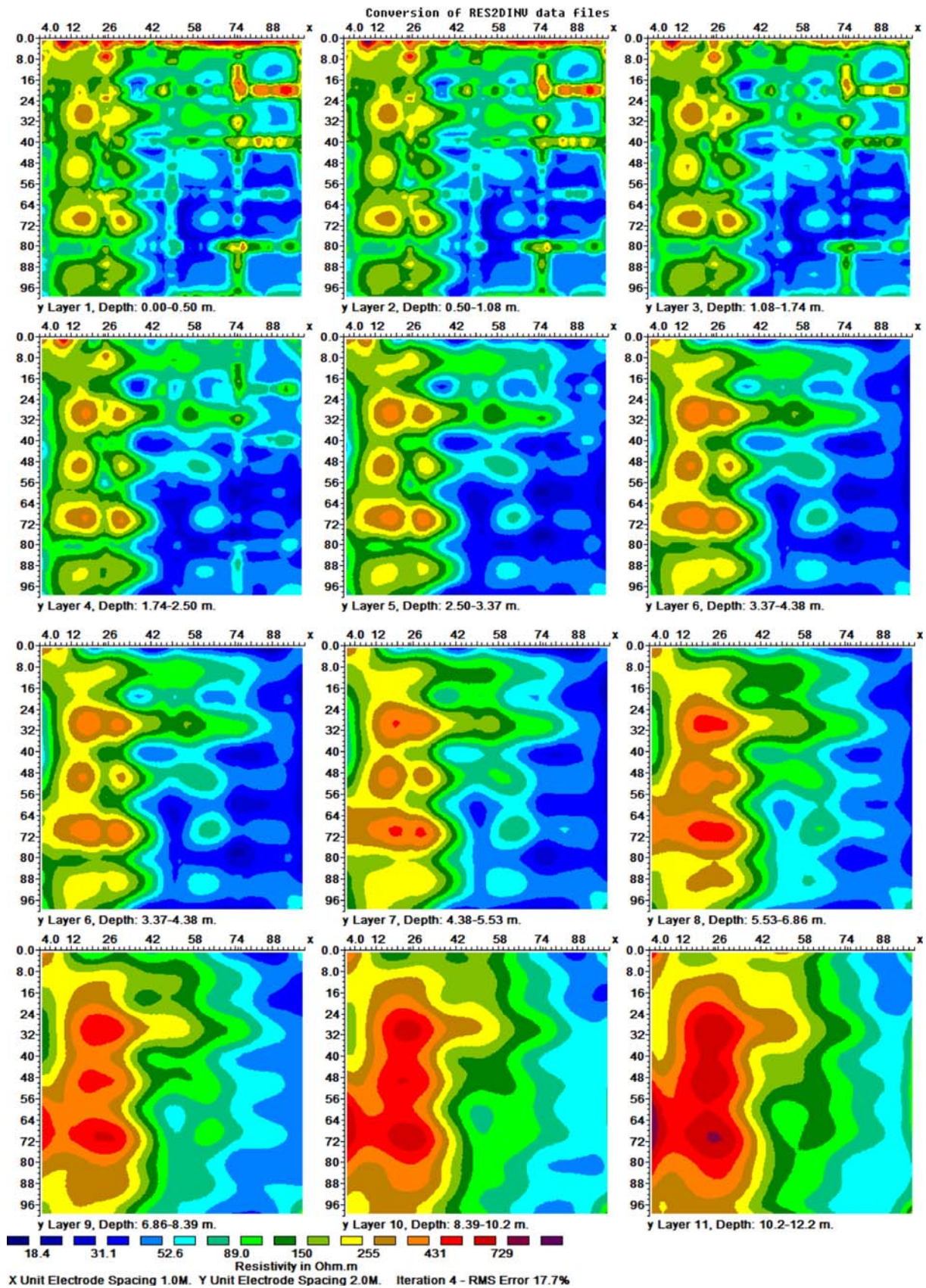
Fig. 8 Horizontal depth slices obtained from the 3D inversion of orthogonal 2D profiles using smoothness constrained least-squares inversion, UI Research Farm, Ibadan, Nigeria
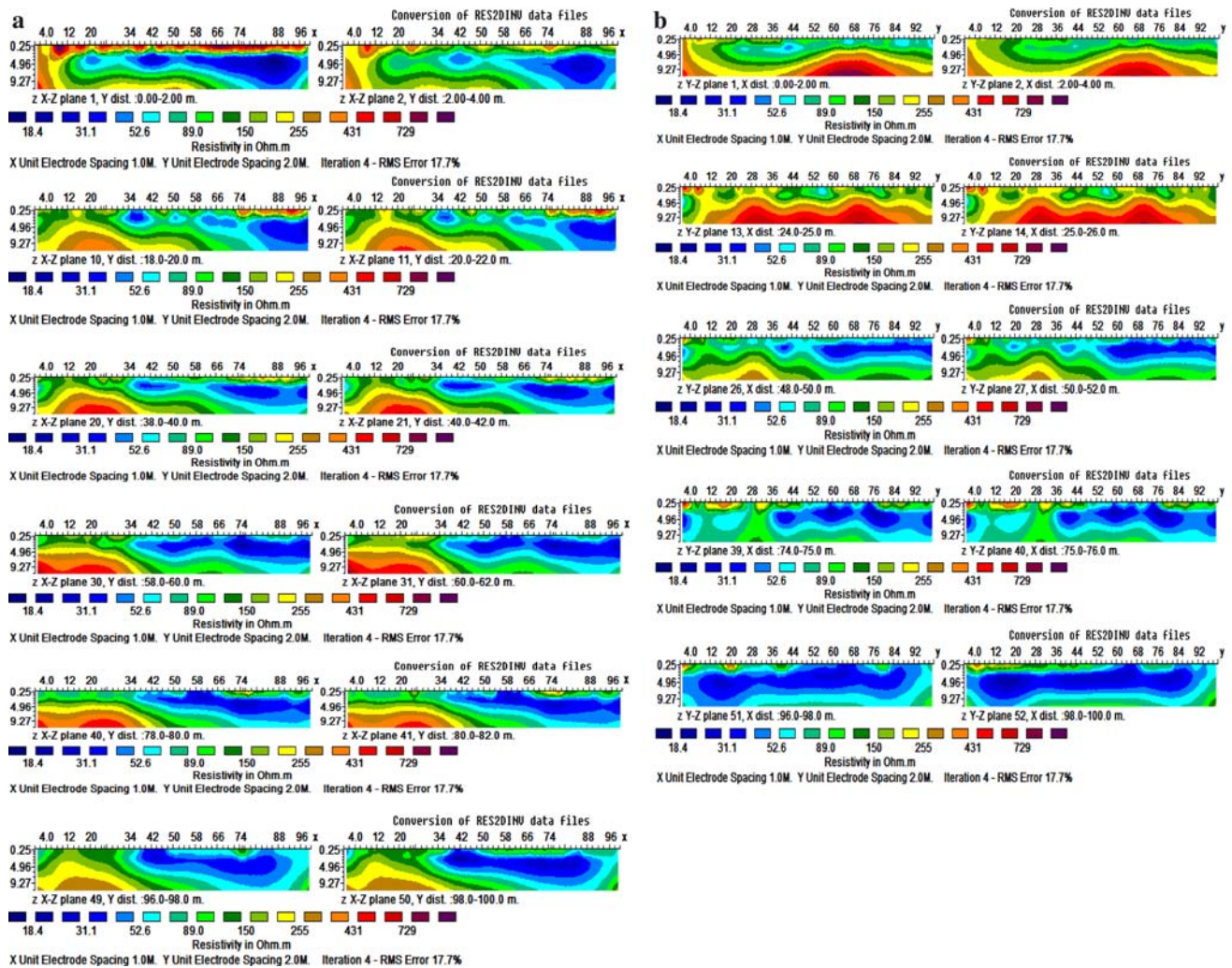
Fig. 9 Extracted 2D images in **a** x–z plane and **b** y–z plane from 3D inversion model coinciding with the 2D profiles measured; each extracted 2D image is at the mid-point between two successive electrodes in the direction perpendicular to the direction of the profile

800 Ωm; unlike a minimum of below 4 Ωm to a maximum of above 18,500 Ωm model values observed in the 2D resistivity images. The trend of the model resistivity values observed in the 3D inversion images are more realistic and feasible compared to that observed in the 2D inversion images. Similarly, distortions and artefacts observed in the 2D images which could be misinterpreted as faults and fractures have been removed in the 3D inversion images. This can clearly seen by comparing the 2D inversion models with 2D images extracted from the 3D inversion models. Hence, the 3D inversion models are superior to the 2D inversion models.

The 2D and 3D geoelectrical resistivity imaging as well as the iso-resistivity contour maps of the VES inverse models revealed the general pattern of resistivity variations within the study area. The 2D and 3D inverse model sections and the iso-resistivity maps show a decrease in

resistivity with depth between the first layer and the second layer with the thickness of the second layer increasing eastward; and an increase in resistivity with depth between the second and the third layer with the resistivity increasing westward. The electrical resistivity of unsaturated porous media depends mainly on the degree of saturation which is a function of the moisture content of the media (Zhou et al. 2001), porosity of the media, and pore-water resistivity. Thus, the variations of subsurface resistivity in the study are due to the variations in these parameters and the degree of weathering and in the weathered profile.

In general, resistivity increases with decreasing porosity, however, electrical properties of subsurface materials are mainly controlled by the quantity and quality of groundwater rather than by the resistivity of the rock matrix (Adepelumi et al. 2001). Thus, the decrease in resistivity with depth between the first and second layers is partly due

to increase in soil moisture down the weathered profile. Similarly, decrease in resistivity eastward in the study area, especially in the second layer (saprolite) which is thought to be an aquifer, is as result of increased weathering activities and the groundwater system flowing in the eastern direction. The increased weathering actions in the eastern part also explain the eastward increase in thickness of the saprolite and the westward increase in model resistivity values with depth between the second and third layers.

Conclusion

Two-dimensional and 3D geoelectrical resistivity imaging has been effectively used in engineering site investigation within the campus of University of Ibadan, southwestern Nigeria. The 3D inversion images increased the degree of reliability of the geoelectrical resistivity imaging. The collation of orthogonal set of 2D apparent resistivity data into 3D data set is fast and effective data acquisition geometry in 3D geoelectrical resistivity survey. Both 2D and 3D inversion models are produced from the observed data set, and are complementary to each other. Unrealistic artefacts and spurious features due to 3D effects commonly associated with 2D inversion images are minimized or completely eliminated in the 3D inversion images. In addition, grid orientation effects are removed by the collation of orthogonal set of 2D profiles. The present study is essentially a near-surface investigation in which a maximum investigation depth of 10.2 m is reached for the 2D and 3D imaging. The resistivity soundings were restricted a maximum half-current electrode spacing of 100 m.

References

Acworth RI (1987) The development of crystalline basement aquifer in a tropical Environment. Q J Eng Geol 20:265–272

Adepelumi AA, Ako BD, Ajayi TR (2001) Groundwater contamination in the basement-complex area of Ile–Ife, southwestern Nigeria: a case study using electrical resistivity method. Hydrogeol J 9:611–622

Akintola JO (1986) Rainfall distribution in Nigeria, 1892–1983. Impact Publishers, Ibadan

Amidu SA, Olayinka AI (2006) Environmental assessment of sewage disposal systems using 2D electrical resistivity imaging and geochemical analysis: a case study from Ibadan, southwestern Nigeria. Environ Eng Geosci 7(3):261–272

Dahlin T, Loke MH (1998) Resolution of 2D Wenner resistivity imaging as assessed by numerical modelling. J Appl Geophys 38(4):237–248

de Groot-Hedlin C, Constable SC (1990) Occam's inversion to generate smooth two-dimensional models from magnetotelluric data. Geophysics 55:1613–1624

Griffiths DH, Barker RD (1993) Two dimensional resistivity imaging and modeling in areas of complex geology. J Appl Geophys 29:211–226

Griffiths DH, Turnbull J, Olayinka AI (1990) Two-dimensional resistivity mapping with a complex controlled array. First Break 8(4):121–129

Li Y, Oldenburg DW (1994) Inversion of 3D DC resistivity data using an approximate inverse mapping. Geophys J Int 116:527–537

Loke MH, Barker RD (1996a) Rapid least-squares inversion of apparent resistivity pseudosections by a quasi-Newton method. Geophys Prospect 44:131–152

Loke MH, Barker RD (1996b) Practical techniques for 3D resistivity surveys and data inversion. Geophys Prospect 44:499–524

Loke MH (2001) Electrical imaging surveys for environmental and engineering studies: a practical guide to 2D and 3D surveys, 62 pp. Available at http://www.geoelectrical.com

Olayinka AI (1999) Advantage of two-dimensional geoelectrical imaging for groundwater prospecting: case study from Ira, southwestern Nigeria. J NAH 10:55–61

Olayinka AI, Yaramanci U (1999) Choice of the best model in 2-D geoelectrical imaging: case study from a waste dump site. Eur J Environ Eng Geophys 3:221–244

Sasaki Y (1992) Resolution of resistivity tomography inferred from numerical simulation. Geophys Prospect 40:453–464

White RMS, Collins S, Denne R, Hee R, Brown P (2001) A new survey design for 3D IP modelling at Copper hill. Explor Geophys 32:152–155

Zhou QY, Shimada J, Sata A (2001) Three-dimensional spatial and temporal monitoring of soil water content using electrical tomography. Water Resour Res 37(2):273–285